10-16-2022

Mountain Rivers Reveal the Earthquake Hazard of Geologic Faults in Silicon Valley

Felipe Aron
Pontificia Universidad Católica de Chile

Samuel A. Johnstone
Stanford University

Andreas Mavrommatis
Stanford University

Robert Sare
Stanford University

Frantz Maerten
Le Lancaster

See next page for additional authors

AGU ADVANCING EARTH AND SPACE SCIENCE

Geophysical Research Letters®

RESEARCH LETTER
10.1029/2022GL099220

Mountain Rivers Reveal the Earthquake Hazard of Geologic Faults in Silicon Valley

Felipe Aron[1,2], Samuel A. Johnstone[2,3], Andreas Mavrommatis[4,5], Robert Sare[2,6], Frantz Maerten[7], John P. Loveless[8], Curtis W. Baden[2], and George E. Hilley[2]

[1]Research Center for Integrated Disaster Risk Management (CIGIDEN) & Departamento de Ingeniería Estructural y Geotécnica, Pontificia Universidad Católica de Chile, Macul, Santiago, Chile, [2]Department of Geological Sciences, Stanford University, Stanford, CA, USA, [3]U.S. Geological Survey, Geosciences and Environmental Change Science Center, Denver, CO, USA, [4]Department of Geophysics, Stanford University, Stanford, CA, USA, [5]Now at Intuit, Mountain View, CA, USA, [6]Now at Google LLC, Mountain View, CA, USA, [7]YouWol, Le Lancaster, Pérols, France, [8]Department of Geosciences, Smith College, Northampton, MA, USA

Abstract The 1989, $M_w = 6.9$ Loma Prieta earthquake resulted in tens of lives lost and cost California almost 3% of its gross domestic product. Despite widespread damage, the earthquake did not clearly rupture the surface, challenging the identification and characterization of these hidden hazards. Here, we show that they can be illuminated by inverting fluvial topography for slip-and moment accrual-rates—fundamental components in earthquake hazard assessments—along relief-generating geologic faults. We applied this technique to thrust faults bounding the mountains along the western side of Silicon Valley in the San Francisco Bay Area, and discovered that these structures may be capable of generating a $M_w = 6.9$ earthquake every 250–300 years based on moment accrual rates. This method may be deployed broadly to evaluate seismic hazard in developing regions with limited geological and geophysical information.

Plain Language Summary Large, shallow earthquakes nucleated along geologic faults promoting vertical motion of rocks produce instantaneous uplift of the Earth's surface on the order of meters. This process and the intervening deformations, repeated over thousands of earthquake cycles, build up mountain ranges, which are subsequently carved by rivers thanks to the action of climate forces counteracting tectonic uplift. Consequently, the incision pattern along mountain rivers, resulting from rock resistance to erosion and long-lived distribution of fault-induced rock uplift, contains information about the past activity of underlying relief-generating faults. Our study tested this fundamental idea, integrating the topography with simple, yet standard mechanical and erosional modeling, to estimate the accrual of earthquake magnitude potential over time. We applied this new methodology, particularly useful to illuminate hazards posed by difficult-to-characterize-faults not well exposed to direct observation, to the fault-bounded mountains along the western side of the San Francisco Bay Area. We discovered that a quake of similar size to the 1989 Loma Prieta event, the last devastating earthquake affecting this populous economic hub, could occur every 250–300 years. More importantly, given the wide availability of topographic datasets, this method may be deployed broadly to evaluate seismic hazards in poorly instrumented and studied areas.

Felipe Aron and George E. Hilley contributed equally to this work.

Key Points:

- The topographic structure of mountain rivers can be inverted for long-term slip-and moment accrual-rates along relief-generating faults
- Thrust faults along the western side of Silicon Valley have the potential for generating a $M_w = 6.9$ earthquake every 250–300 years
- This approach may be deployed more broadly to evaluate seismic hazard in regions with limited geological and geophysical information

Supporting Information:

Supporting Information may be found in the online version of this article.

Correspondence to:

F. Aron,
faron@ing.puc.cl

Citation:

Aron, F., Johnstone, S. A., Mavrommatis, A., Sare, R., Maerten, F., Loveless, J. P., et al. (2022). Mountain rivers reveal the earthquake hazard of geologic faults in Silicon Valley. *Geophysical Research Letters*, *49*, e2022GL099220. https://doi.org/10.1029/2022GL099220

Received 27 APR 2022
Accepted 22 AUG 2022

Author Contributions:

Conceptualization: Felipe Aron, Samuel A. Johnstone, George E. Hilley
Data curation: Felipe Aron, George E. Hilley
Formal analysis: Felipe Aron, Samuel A. Johnstone, Andreas Mavrommatis, Robert Sare, George E. Hilley
Funding acquisition: Felipe Aron, George E. Hilley
Investigation: Felipe Aron, Samuel A. Johnstone, Andreas Mavrommatis, Robert Sare, Frantz Maerten, John P. Loveless, Curtis W. Baden, George E. Hilley
Methodology: Felipe Aron, Samuel A. Johnstone, Andreas Mavrommatis, Robert Sare, Frantz Maerten, John P. Loveless, Curtis W. Baden, George E. Hilley

1. Introduction

The last major earthquake ($M_w = 6.9$) to strike the San Francisco Bay Area in 1989 killed 63 people, injured thousands, and cost upwards of $20.5 billion in 2021 US dollars (U. S. Geological Survey Staff, 1990; National Research Council, 1994). The greater Bay Area now hosts almost 2 million, or ∼29% more people than it did in 1989 (according to stats from the "Bay Area Census," 2020; and the "State of California Department of Finance," 2020), making it the world's 19th largest economy when viewed as a sovereign nation (Bay Area Council Economic Institute, 2018). Yet, this growth has occurred within an area where a complex array of strike-slip and reverse faults are capable of generating large, damaging earthquakes (Field et al., 2017; Sykes & Jaumé, 1990). Hazards posed by many of these faults can be assessed directly using space geodesy (Segall & Lisowski, 1990), historic seismicity (Ellsworth, 1990), and paleoseismology (Schwartz et al., 1998, 2014). But many hazards within this area may result from motion along reverse faults, whose geometries and lack of surface-rupturing earthquakes make them particularly difficult to characterize (McCalpin, 2009), posing some of the highest risks to the region and, by extension, the national economy. While conventional methods may fail

Project Administration: Felipe Aron, George E. Hilley
Resources: Felipe Aron, Samuel A. Johnstone, Curtis W. Baden, George E. Hilley
Software: Felipe Aron, Samuel A. Johnstone, Andreas Mavrommatis, Robert Sare, Frantz Maerten, John P. Loveless, George E. Hilley
Supervision: Felipe Aron, George E. Hilley
Validation: Felipe Aron, George E. Hilley
Visualization: Felipe Aron, Samuel A. Johnstone, George E. Hilley
Writing – original draft: Felipe Aron, Samuel A. Johnstone, Andreas Mavrommatis, Robert Sare, Frantz Maerten, John P. Loveless, Curtis W. Baden, George E. Hilley
Writing – review & editing: Felipe Aron, Samuel A. Johnstone, John P. Loveless, George E. Hilley

to delineate these hidden threats, the topography that has been built by slip along crustal faults should contain important information about rates at which seismic moment may be accruing. Our contribution tests this fundamental idea, using the topography with mechanical and erosional modeling to estimate moment accrual-rates—a primary input to any probabilistic seismic hazard assessment—along reverse faults of the western Bay Area.

2. Background and Methods

2.1. The Santa Cruz Mountains Restraining Bend and the Sierra Azul

We focus our modeling on the Shannon-Monte Vista and Berrocal-Sargent fault zones (hereafter referred to as the Foothills Thrust Belt or FTB, Figure 1), which are thought to be capable of producing a $M_w = 7.1$ earthquake (Bürgmann et al., 1994, 1997; Field et al., 2017; Hitchcock & Kelson, 1999; Mclaughlin et al., 1999; Tuttle & Sykes, 1992; Yu & Segall, 1996). These reverse faults have apparently formed due to an ∼11° left-bend in the San Andreas Fault, which converts shearing into contraction (Anderson, 1990, 1994; Aydin & Page, 1984) and leads to the construction of the >1.2-km-high Southern Santa Cruz Mountains or Sierra Azul (hereafter referred to as SA) (Figure 1). While the Pacific Block has been advected through the restraining bend, the North American (Bay) Block has remained relatively immobile (Baden et al., 2022). The most recent recorded significant earthquake that may have occurred along these structures, of $M = 6.5$, was in 1865 A.D. (Ellsworth, 1990; Tuttle & Sykes, 1992; Yu & Segall, 1996). However, knowledge of the frequency of these and larger earthquakes is limited by the unfavorable geometry of the faults for performing paleoseismology studies, urban development in the area, and a lack of earthquake-related deposits, all of which hamper efforts to understand rates at which seismic moment may be accruing. Fault-offset terraces, which serve as markers of past river levels, and piedmont deposits provide some information about their Quaternary slip rates (∼0.45 mm/a) (Hitchcock & Kelson, 1999; Mclaughlin et al., 1999), but the location of available sites and a lack of age control obscures the potential hazard that they pose.

Previous geologic mapping and geophysical imaging constrain the surface outcroppings of rocks and subsurface geometries of faults (see Supporting Information S1). Slip along the range-bounding thrusts (Mclaughlin et al., 1999) has caused average rock uplift-rates of ∼0.8–1.2 mm/a over the last 4 Ma in the southern area (Bürgmann et al., 1994) (Figure 1a). This uplift stands in contrast to adjacent areas located northeast of the range, where thick Pliocene-Holocene deposits of the Santa Clara Valley indicate stability, and possibly subsidence during this time (Langenheim et al., 2015). Elevations within the SA reach their maximum at locations where the bend in the San Andreas Fault is tightest, decreasing to the northwest and southeast of these areas (Figure 1a) (Anderson, 1994). Within this broad pattern, we expect that topography is generally steeper in rock types thought to be more resistant to erosion (e.g., well-indurated sandstones) than in, for example, mudstones (Stock & Montgomery, 1999). Together, these observations indicate that topography within the SA depends on: (a) the rates of rock uplift caused by the bounding reverse faults that slip in response to strike-slip motion along the San Andreas Fault, as well as (b) the distribution of rock-types exposed to erosion within the range (Figure 1).

2.2. A Model Coupling Geomorphology With Plate Motion

Complementary theories exist for predicting both of the aforementioned factors. Boundary Element Method (BEM) models can estimate how plate motion is partitioned between faults within the crust, and predict how fault slip uplifts rocks near the surface (e.g., Marshall et al., 2009). The stream power incision rule predicts how erosion rates, assumed equal to uplift-rate, vary with watershed area, channel slope and resistance of exposed rocks (Stock & Montgomery, 1999; Whipple & Tucker, 1999). We combine these theories with a nonlinear inversion scheme (see Supporting Information S1) to estimate far-field, long-term plate motions responsible for slip along structures surrounding the San Andreas Fault, and the erodibility of the exposed rock-types (Graymer et al., 2006), based on observed channel elevations within the SA (Figure 1). First, we used published geologic mapping and geophysical imaging to discretize the geometry of these structures and assemble a 3D triangular mesh (refined to achieve mesh-resolution independent results) to be input in the BEM code tribemx (Figure 1c; see Supporting Information S1; Figures S1 and S2; Data Set S1 in Supporting Information S1). Faults are represented as traction-free surfaces embedded in an elastic half-space free of gravitational loads, and are not allowed to displace in the element-normal direction. This boundary condition imposes a strike-and dip-slip displacement along the faults, with a rate that depends on the geometry of the model and on the imposed far-field load. In the

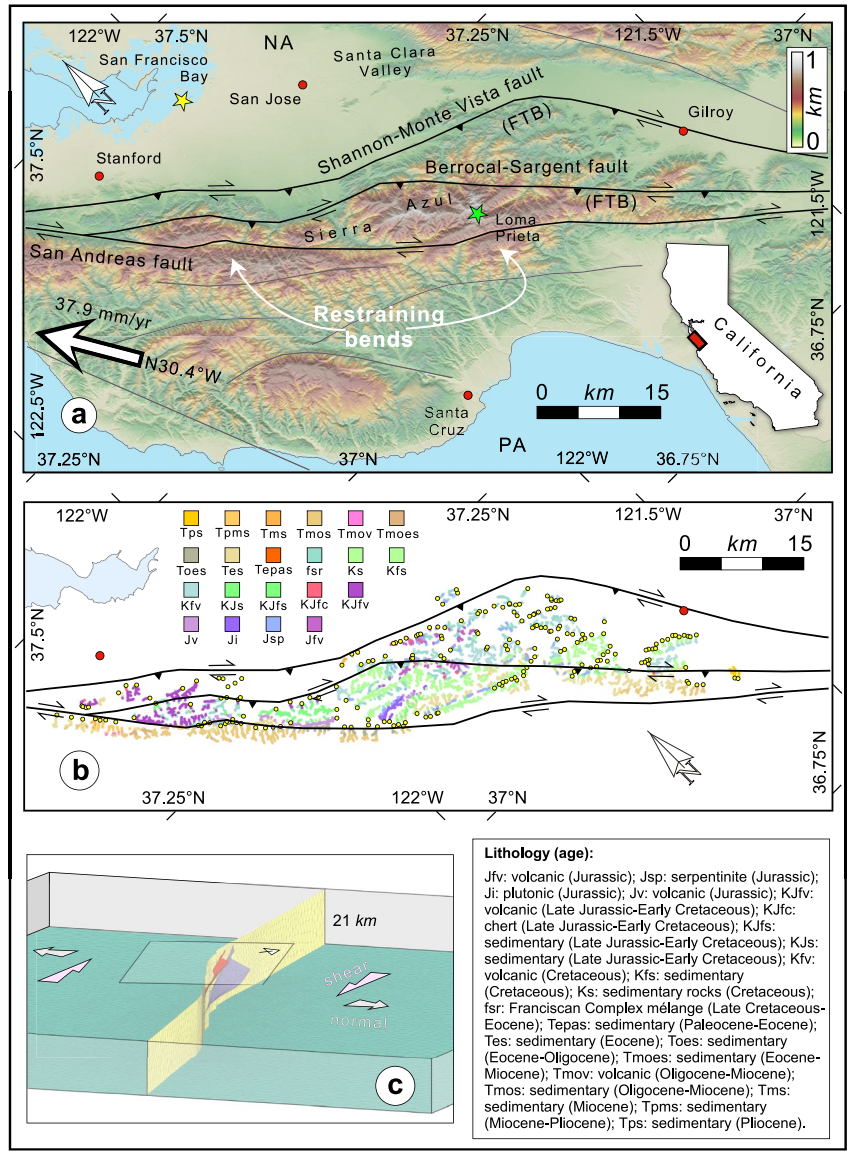

Figure 1. Tectonic and geologic setting. (a) Tectonic, structural and morphological configuration of the Santa Cruz Mountains restraining bends of the San Andreas Fault. Thick black curves are traces of the San Andreas and Foothills Thrust Belt (FTB) (Berrocal-Sargent and Shannon-Monte Vista) faults modeled in this study; thin gray lines correspond to other faults mapped in the region. Large black-white arrow shows geologic, relative motion vector between North American (NA; stable) and Pacific (PA) plates (Argus et al., 2011). Green and yellow stars denote the locations where long-term, rock uplift-rates have been measured in the Sierra Azul (SA) (Bürgmann et al., 1994) and Bay Area (Langenheim et al., 2015), respectively. Colorbar shows elevation. (b) Map centered at the SA showing all measured channel points color-coded by lithology (Graymer et al., 2006). Text inset below explains rock-type and age for the 21 bedrock lithologic classes used to constrain erodibility (K in Equation 1). Yellow circles are the outlets of all the identified channels (n_{out} = 220). (c) 3-D view to the north-west showing the geometric arrangement of faults (see also Figure S1 in Supporting Information S1) used to compute Green functions of slip-rates and rock uplift-rate (U) in response to prescribed, far-field plate motion $\vec{v}$ (Equation 1; with $\boldsymbol{v}_s$ shear [+right-lateral] and $\boldsymbol{v}_n$ normal [+extension] components). Horizontal semi-transparent rectangle (with north arrow) outlines the area shown in (a).

forward problem, far-field displacement rates prescribed along the edge of the model ($\vec{v}$ [L/t]) simulate plate motion and excite slip along these structures via a horizontal, traction-free lower boundary that is not allowed to displace in the vertical direction (Figure 1c; Figure S1 in Supporting Information S1) (e.g., Marshall et al., 2009). This configuration is used to construct Greens functions relating plate motion to vertical displacement rates ($\boldsymbol{U}$ [L/t]) at all channel points. By explicitly prescribing the surfaces of the FTB faults for modeling topographic

growth and crustal deformation along the plate boundary, we provide an alternative strategy to others that account for strain-hardening, plastic yielding, and isostatic and flexural compensation, in the absence of relief-bounding, subsidiary faults (e.g., Baden et al., 2022). Next, the publicly available, 10-m-resolution National Elevation Data set Digital Elevation Model (DEM) was used to route flow over the topography by filling internal sinks before calculating watershed area (A [L^2]), which is in turn used to identify all measured channel elevation points (z_m [L]) in the SA, defined as having catchment areas >0.1 km^2 (see Supporting Information S1; Figure S3; Data Set S2 in Supporting Information S1). By assuming that channel incision rates balance uplift, we employ the power-law river incision model to predict channel bed elevations at each point (z_p [L]) as (Goren et al., 2014; Perron & Royden, 2013):

$$z_p(\vec{x}) = z_o + \int_{\vec{x_o}}^{\vec{x}} \left(\frac{U(\vec{\psi}|\vec{v})}{K(\vec{\psi}|G)} \right)^{1/n} A(\vec{\psi})^{-\theta} d\vec{\psi}, \quad (1)$$

where z_o [L] is a specified outlet elevation measured from the DEM at $\vec{x_o}$ of each independent channel (Data Set S2 in Supporting Information S1), K (rock erodibility [$L^{1-2\theta n}$/t]) is an empirical constant that mainly encapsulates the impact of rock type (G) on incision rate, θ is an empirically measured or specified channel concavity constant (typically in the range of 0.2–0.6; Figure S3 in Supporting Information S1), and n is the slope exponent of the power-law incision model, which is thought to depend on the mechanics of channel erosional processes (see Supporting Information S1). The integral in Equation 1 is evaluated along the channel segment connecting all upstream points in a designated watershed ($\vec{x}$; Cartesian coordinates) to their corresponding downstream outlet ($\vec{x_o}$) as they traverse points along each flowpath ($\vec{\psi}$; along-path coordinates). By setting $\theta = 0.4$, in accordance with current topography (Figure S3 in Supporting Information S1) and n equal to unity (see Supporting Information S1), necessary to compare our model predictions with independently estimated rock erodibilities on similar rocks (Stock & Montgomery, 1999), z_p can thus be calculated at each point in a watershed, assuming the spatial distributions of rock types ($K(\vec{\psi})$) and uplift-rates ($U(\vec{\psi})$) are known. Our selection of n and θ resulted in values of channel steepness below the global threshold identified by Hilley et al. (2019) using the same scaling exponents, above which steepness becomes insensitive to erosion rate, meaning that the power-law incision rule is likely a valid approximation for the SA river elevation structure (Figure S4 in Supporting Information S1).

Alternatively, Equation 1 can be posed as an inverse problem in which the misfit between z_m and z_p is used to estimate U (and therefore $\vec{v}$) and K values associated with mapped surface exposures of rock-type classes (G, assumed uniform within each class; Figure 1b), as well as the constant of integration z_o. Because K is in the denominator of Equation 1, we separated the problem into its linear and nonlinear components to approximate the joint distribution of these parameters, which can be later used to assess the uncertainty within and uniqueness of K and $\vec{v}$, erodibilities and plate rates (see Supporting Information S1). This methodology can thus be used to reveal the set of $\vec{v}$ and $K(G)$ that reproduces the observed topography (z_m) as well as to calculate the resulting distribution of rates of slip and moment accrual along faults—and so, $U(\vec{\psi})$ across the SA that produced the observed topography.

3. Results

3.1. Best-Fit Plate Velocity, Rock Erodibilities, Fault Slip-Rates, and Rock Uplift-Rates

We applied this approach to the FTB by matching measured and predicted channel elevations observed in the SA (Figure 2), while penalizing uplift within the current location of the San Francisco Bay shore (Langenheim et al., 2015), and discordance between measured (Bürgmann et al., 1994) and predicted, long-term rock uplift-rates in the SA (stars in Figure 1a)—both the sole constraints applied to the inversion (see Supporting Information S1). When uplift-rates within the Bay and SA were strongly enforced (*preferred model*; see Supporting Information S1; Figures S9–S13 in Supporting Information S1), and assuming geomorphic steady-state with $n = 1$ (see Supporting Information S1; Figures S5–S8 in Supporting Information S1), we found that $v_s = 16.25 \pm 0.02$ mm/a and $v_n = -0.15 \pm 0.02$ mm/a, the shear (+right-lateral), oriented parallel to the relative plate motion vector shown in Figure 1, and normal (+extension) components of $\vec{v}$, respectively (range denote $\pm 2\sigma$ intervals; Figure 1c; Figure S1 in Supporting Information S1)—virtually identical to rates derived from geodetic inversions, mechanical modeling and paleoseismologic studies (Table S1 in Supporting Information S1) (Argus &

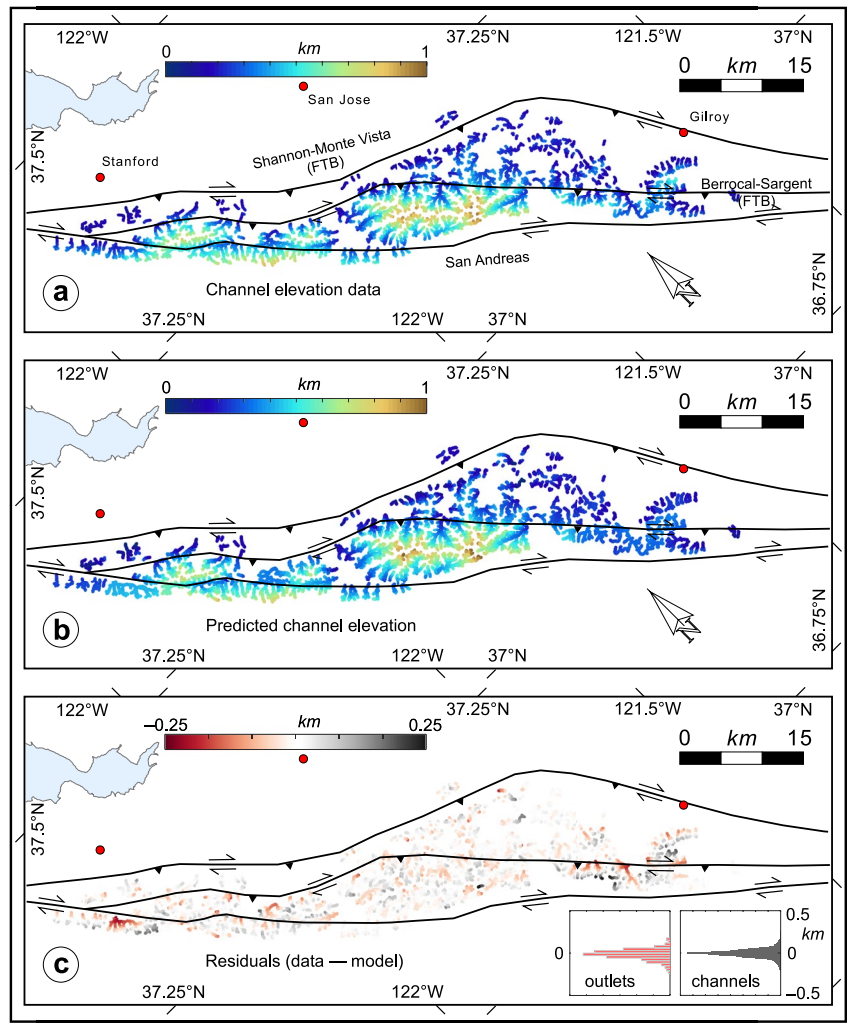

Figure 2. Fit to the data. Maps of the SA showing model fit (maximum-likelihood scenario) to channel elevation data resulting from strongly enforcing the uplift-rate constraints (*preferred model*; see Supporting Information S1; compare to Figures S11 and S12 in Supporting Information S1). (a) Data (10-m-resolution National Elevation Data set Digital Elevation Model); (b) model; and (c) residuals (data — model). Insets show histogram of residuals for channel (gray) and outlets (z_o; red) elevation, with mean/standard deviations = −2.7/50.7 m, and −16.8/58.9 m, respectively.

Gordon, 2001; d'Alessio et al., 2005; Evans et al., 2012; Field et al., 2017; Johnson & Fukuda, 2010; Murray & Segall, 2001; Prescott et al., 1981; Savage et al., 1999). The maximum-likelihood scenario of the far-field rates produces ∼1.1–1.5 mm/a of area-weighted, average slip-rate along the faults of the FTB (Figure 3; Figure S14 in Supporting Information S1), which ultimately yield rock uplift-rates that are on average 0.5 mm/a within the SA (Figure 4a; Figure S15 in Supporting Information S1), coincident with the findings by Prescott and Burford (1976) and Bürgmann et al. (1994). Simple models of channel incision suggest that their forms approximately record the amount of time required to uplift rock over a height equal to the vertical relief of channels (Whipple & Tucker, 1999). We estimate this to be ∼0.6–1 Ma in the SA case, using the altitude of high peaks and rock uplift-rates ranging between 800 and 1000 m (Figure 2a), and 1–1.2 mm/a (Figure 4a), respectively. The modeled fault slip-rates in this study thus represent averaged rates over these time-scales. Interestingly, the $[10^{-5.1}, 10^{-4.4}]$ $m^{0.2}$/a range of estimated erodibility values of all bedrock lithologic classes also falls within the broad range observed in nature for $n = 1$ (Stock & Montgomery, 1999), which provides some independent validation of the approach (see Supporting Information S1; Tables S1 and S2 in Supporting Information S1). Taking $\boldsymbol{n} = 2/3$ or 2.5 does not yield a significant impact in fault slip-rate determination, and so moment accrual-rates, as the primary sensitivity of the model to the slope exponent is in the values of K (see Supporting Information S1;

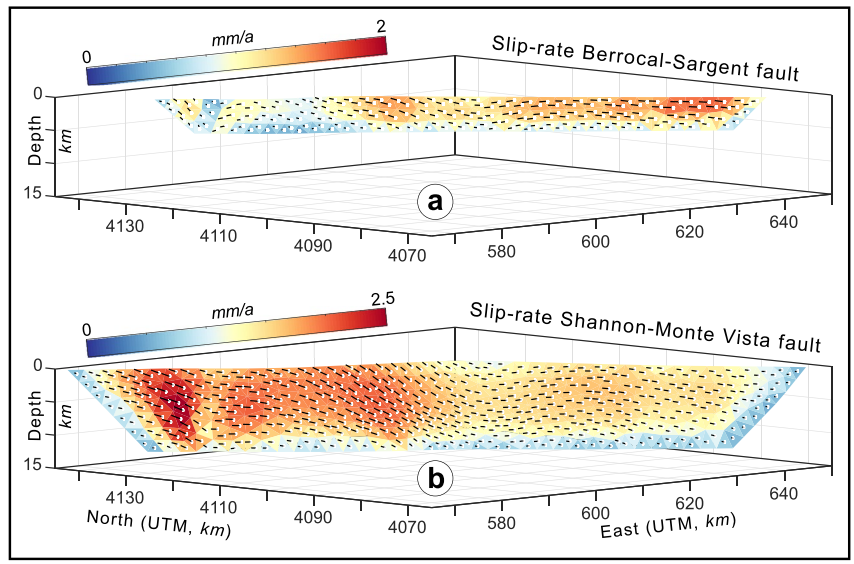

Figure 3. Foothills Thrust Belt long-term fault slip-rates. 3-D views to the north-east showing fault slip-rate distribution along the (a) Berrocal-Sargent, and (b) Shannon-Monte Vista faults, computed using maximum-likelihood results of the *preferred model* (see Supporting Information S1; compare to Figure S14 in Supporting Information S1). Black lines depict slip-rate vectors (origin denoted by white dots at triangle centroids). Note that long-term slip-rate concentrates in portions of the fault that could constitute long-term asperities. We hypothesize that those regions are more prone to develop large static slip during earthquakes.

Table S5 in Supporting Information S1). The order of magnitude of the plate rates is set by the constraints and the erodibilities have to adjust to maintain the fixed, measured relief.

3.2. Discrepancies With Observations

The differences between the observed and predicted channel elevations of the maximum-likelihood model, hereafter referred to as residuals, are systematically larger within two localized patches at the northwestern and southeastern portions of the model than elsewhere (Figure 2; Figures S11–S13 in Supporting Information S1). Residuals appear largest where topography is present along strike-slip faults that lack restraining bends, which likely reflects the simplifications and errors in the fault geometry model (e.g., Marshall et al., 2009), or localized lateral offset of channels produced by fault strike-slip motion (Figure 3) (Prescott & Burford, 1976), not explained by the uplift-dependent, power-law river incision model. Nonetheless, slow slip-rates along the FTB faults should facilitate ridge migration and/or stream capture, so the landscape response to the disequilibrium brought about by strike-slip motion obscures the effect of river lengthening and deflection, preserving the overall trajectories of channels across the faults (Duvall & Tucker, 2015). If one assumes a range of strike-slip motion along the FTB faults of 1.1–2 mm/a (Figure 3) these structures should have produced 0.7–2 km of lateral motion over the last 0.6–1 Ma. The magnitudes of these potential movements are far smaller than the wavelength of the uplift-rate signal predicted by the mechanical model. Thus, the assumption of a stationary geometry appears to be approximately valid. Alternatively, high residuals could be the result of transient topography (Whipple & Tucker, 1999) or planform changes of the river network due to water divide migration (Castelltort et al., 2012), also not accounted for in our model. Perhaps erodibility variations not captured by the geologic map or caused by rainfall gradients across the mountain range, which in the SA can be as large as 500–600 mm of average annual precipitation between the higher peaks and the lowlands ("Average annual precipitation for California, USA (1900–1960) | Data Basin," 2022), may impose further limitations to our approach. Another important source of error is the epistemic uncertainty or model appropriateness. The standard deviation of the model residuals is about three times the reported error of the SRTM elevation measurements (Figure 2). This most likely relates to simplifications in the model relative to the complexities of the natural system (see Supporting Information S1). In any case, even with a threefold increase in the error of the inverted parameters, their quantities fall within the observed, natural range (Table S1 in Supporting Information S1).

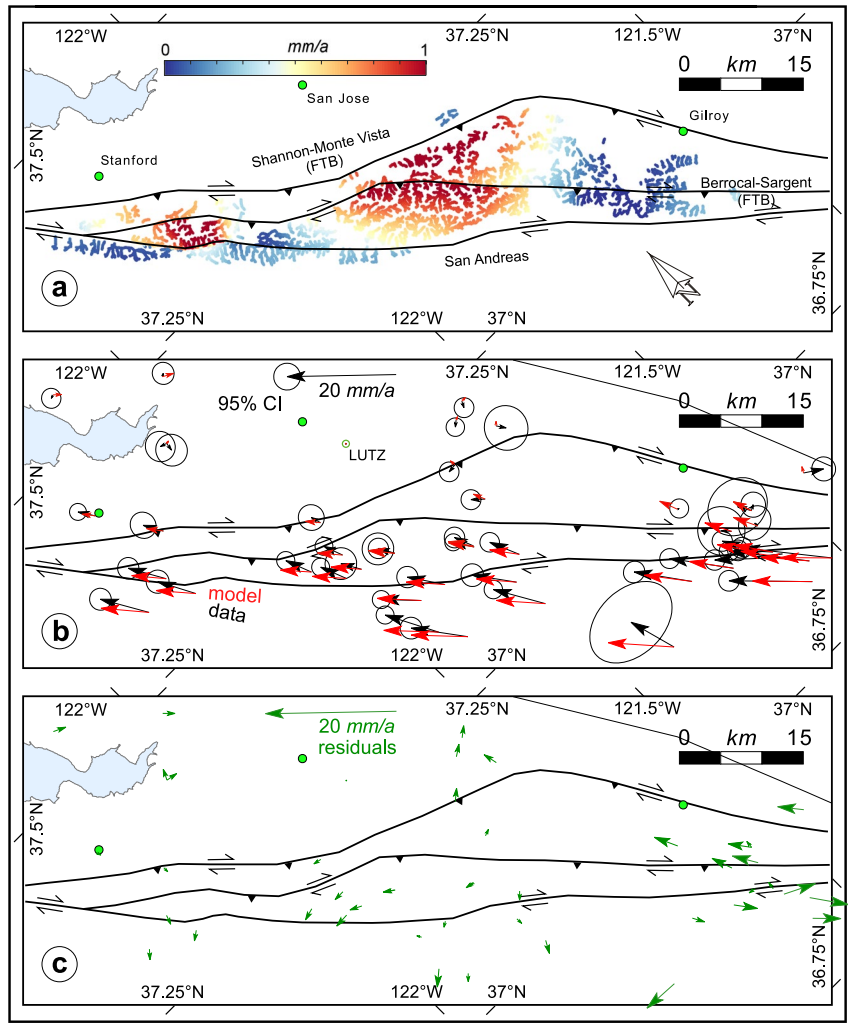

Figure 4. Long-term and interseismic surface deformation across the SA. (a) Map showing rock uplift-rate distribution over the SA channels computed using maximum-likelihood scenario of the *preferred model* (see Supporting Information S1; compare to Figure S15 in Supporting Information S1). (b) Horizontal interseismic surface velocities at Bay Area continuous GPS network, referred to LUTZ station for comparison with velocities reported by d'Alessio et al. (2005). Black and red arrows are, respectively, observed (with 95% confidence intervals ellipses) and predicted velocities from composite slip model adjusted for the effect of locked faults. (c) Residuals of velocities shown in B (data — model). Larger misfits observed in the south-eastern portion are coincident with larger discrepancies between modeled and measured channel elevations (Figure 2). Additionally, unmodeled surface creep may cause observed velocities to abruptly change across the structure.

Regardless of those potential limitations, residuals are normally distributed with a mean around zero within the input data error, showing no apparent systematic deviations. The magnitude of these differences expressed as the standard deviation of the residuals, including that of predicted versus observed outlet elevation (z_o), are only a fraction of the total elevation range across the area (Figure 2; Figures S11–S13 in Supporting Information S1). Thus, the topography observed within the SA requires slip-rates and erodibility values that appear to be consistent with available geologic, paleoseismic, and geodetic information from the region. We therefore conclude that the assumption of geomorphic steady-state and selection of power law exponents (θ and n), chosen partly to enable comparison with independent measurements, are adequate for integrating the geomorphic and mechanical models.

3.3. Long-Versus Short-Term Plate Motion and Surface Deformation

We provide a further test by determining how well the maximum-likelihood scenario of the *preferred model* reproduced current, interseismic surface motions measured at GPS stations (Figure 4b). To do this, we first

calculated surface velocities at each GPS site within the greater Bay Area (d'Alessio et al., 2005), applying our preferred $\vec{v}$ estimation to the BEM model of the restraining bend faults. From these velocities, we then subtract the surface motion computed from reversed estimated slip along the upper 10 km of all modeled faults, thereby simulating the effect of interseismically locked faults. Finally, we calculated the contribution of other faults within the Bay Area to surface velocities using the geometries, locking depths, and slip-rates estimated for these structures (d'Alessio et al., 2005). The resulting surface velocity field closely matches that observed over decades, despite the large difference in time-scales (Figures 4b and 4c). The relatively high residuals observed in the southeastern side could be caused by unmodeled fault creep in that section of the Sargent fault (Mongovin & Philibosian, 2021; Turner et al., 2013).

3.4. Moment Accrual-Rates and Slip-Predictable, Earthquake Size Estimations

The modeled slip rates along the FTB bound the maximum rate at which seismic moment may be accruing, in the absence of other significant stress release processes such as creep. We determined this rate to be 9.2×10^{23} dyne-cm/a by integrating slip-rate magnitude of our *preferred solution* over the two modeled FTB faults, using a uniform shear modulus of 32 GPa (7.4×10^{23} and 1.8×10^{23} dyne-cm/a for the Shannon-Monte Vista and Berrocal-Sargent faults, respectively, Table S3 in Supporting Information S1; see Supporting Information S1). If all of this accrued moment were to be released in a single earthquake rupturing the faults of the FTB, and assuming a slip-predictable earthquake model (Shimazaki & Nakata, 1980), a Loma Prieta-type event ($M_w = 6.9$) could be generated along these structures every 250–300 years or a $M_w = 7.0$ earthquake every 350–400 years (Table S4 in Supporting Information S1). As a point of reference, the 1865 A.D. event, which occurred 157 years ago, is thought to have been a $M = 6.5$ earthquake (Ellsworth, 1990; Tuttle & Sykes, 1992; Yu & Segall, 1996); our estimates of recurrence times for that magnitude range between 100 and 150 years (Table S4 in Supporting Information S1).

4. Discussion and Conclusions

Correspondence between mapped rock types within the SA (Graymer et al., 2006) and independent calibrations of erodibilities in similar rock types (Tables S1 and S2 in Supporting Information S1) (Stock & Montgomery, 1999), as well as modeled and observed interseismic velocities (Figures 4b and 4c) (d'Alessio et al., 2005), validate this new approach, regardless of the simplifications and assumptions required for coupling the mechanical and geomorphic models (see Supporting Information S1). These tests were possible because earthquake hazards threatening the Bay Area have motivated detailed geologic mapping and extensive geodetic instrumentation across the region. Nonetheless, it is unclear whether this approach might only be applied to these well-studied regions, or might be broadly useful for characterizing the risks faced by developing, urbanized areas, where geophysical and geologic data are often in short supply. To gauge its usefulness, we explored a scenario in which moment accrual-rates were inferred based on a set of simplified fault geometries (Figure S16 in Supporting Information S1) and no existing geologic mapping (see Supporting Information S1). Using a single erodibility parameter, representing an area-weighted average for the mountain range, we found that moment accrual-rates at the FTB are 8.9×10^{23} dyne-cm/a for the *preferred model* constraints. The broad, yet remarkable consistency between data-rich and data-poor model results suggests that the ultimate objective of this analysis—the estimation of moment accrual-rates along difficult-to-characterize structures—may not require sophisticated geologic mapping nor geophysical imaging. Alternatively, this may reflect that the inferred erodibilities of different rock types in this region overlap. Independent geologic mapping and geophysical studies reduce epistemic uncertainty by identifying fault geometry and lithologically-induced variations in channel steepness. We also acknowledge that the predictive power of our elastic, quasi-static, fixed-geometry mechanical, and constant-uplift geomorphic models can be improved, for instance, by accounting for: (a) long-term planform modifications of river networks (Castelltort et al., 2012), (b) time variations of uplift-rate (Goren et al., 2014; Steer, 2021), and (c) material yielding and block advection (Baden et al., 2022), particularly in tectonic environments dominated by lateral motion. Nevertheless, our inversion approach might be used as a starting point in areas where sparse geodetic and geologic information may leave geoscientists with few other tools for constraining seismic hazard. Further, our approach can be easily tested against measurements of catchment-averaged erosion rates and thermochronologic ages, both quantities that can be extracted from the proposed integrated model. The primary dependence of our

method on widely available topography data sets, as well as the simple nature of the coupled mechanical-erosion model, enables intuitive interpretation of the first-order parameters that govern a region's seismic hazard.

Topography likely records fault activity over periods of time that bridge geodetic (i.e., decades) and geologic (i.e., Ma) observations (Kirby & Whipple, 2012). This leads us to two conclusions. First, the success of the approach in reproducing interseismic surface velocities suggests that moment may be accruing, more-or-less constantly, over these time periods. Consequently, our results indicate that within the SA it is possible to reconcile geologic (10^6 a), topographic (10^{5-6} a), paleoseismic (10^{2-3} a), and geodetic (10^{1-2} a) observations of plate motion, fault slip and surface displacements—a fundamental and outstanding problem in tectonics (Pollard & with 25 community contributors, 2003; Tikoff et al., 2013; Huntington et al., 2018). Second, the last probable damaging earthquake along these structures occurred in 1865. Given that the maximum moment accrual rate is capable of producing a $M_w = 6.9$ event along the FTB every 250–300 years—or a $M_w = 6.5$ every 100–150 years—it appears that these structures have the potential to cause severe shaking in the adjacent Santa Clara Valley, that could result in major human and economic loss.

Conflict of Interest

The authors declare no conflicts of interest relevant to this study.

Data Availability Statement

For purposes of reproducing or extending the analysis, all data, algorithms, code and methods are available in the main text, and Supporting Information S1, or at referenced scientific and/or public sources. The faults triangular meshes data (Data Set S1 in Supporting Information S1), used in the boundary elements mechanical model, and the locations and elevations of all the channel and outlet points of the river network across the Sierra Azul (Data Set S2 in Supporting Information S1), used as input data in the inversion, are available at Repositorio UC via https://doi.org/10.7764/datasetUC/ING/64714 with Creative Commons Attribution-NonCommercial-ShareAlike 4.0 International Public License. Mechanical models to generate uplift-rate Greens functions were run with the open source boundary elements method code tribem: Boundary element code using triangular dislocation elements (Loveless, 2019), available at https://doi.org/10.5281/zenodo.3333899. The model input faults and boundary surfaces (Data Set S1 in Supporting Information S1) were meshed using the open source code Gmsh© (Geuzaine & Remacle, 2009), available at https://gmsh.info/. Geographically referenced files of the geologic map of the San Francisco Bay Region by Graymer et al. (2006) were used to geotag all channel points (Data Set S2 in Supporting Information S1) with its corresponding lithology, which is freely available at https://doi.org/10.3133/sim2918. Channel point elevations were extracted from the 1/3rd arc-second Digital Elevation Models (DEMs)—U.S. Geological Survey (USGS) National Map 3DEP Downloadable Data Collection, available at https://www.sciencebase.gov/catalog/item/4f70aa9fe4b058caae3f8de5. The algorithms to compute the inverse problem and model uncertainty presented in this article were scripted using licensed copies of Matlab© and Python©.

Acknowledgments
The authors would like to thank Stephen DeLong, Matt Fox, Dave Pollard, Paul Segall, Peter Molnar (R.I.P.), Bob McLaughlin, W. Ashley Griffith, and Laurent Maerten for providing their insight about the methods and scientific aspects of this work. The results obtained and conclusions expressed here may not necessarily represent their views. The authors also thank the thoughtful and constructive reviews and recommendations by Philippe Steer, Mike Oskin, Steve DeLong, Editor Germán Prieto, and an anonymous reviewer, which helped us to clarify the methods, model limitations and constraints, and the significance of our results. Disclaimer: Any use of trade, firm, or product names is for descriptive purposes only and does not imply endorsement by the U.S. Government. FA acknowledges support from ANID Fondo Nacional de Desarrollo Científico y Tecnológico (FONDECYT-Chile) grant 3150116 and Fondo de Financiamiento de Centros de Investigación en Áreas Prioritarias ANID/FONDAP/15110017-Chile (CIGIDEN). GEH acknowledges support from NSF Career Grant EAR-TECT-105581.

References

Anderson, R. S. (1990). Evolution of the northern Santa Cruz Mountains by advection of crust past a San Andreas Fault bend. *Science*, *249*(4967), 397–401. https://doi.org/10.1126/science.249.4967.397

Anderson, R. S. (1994). Evolution of the Santa Cruz Mountains, California, through tectonic growth and geomorphic decay. *Journal of Geophysical Research*, *99*(B10), 20161–20179. https://doi.org/10.1029/94JB00713

Argus, D. F., & Gordon, R. G. (2001). Present tectonic motion across the Coast Ranges and San Andreas Fault system in central California. *The Geological Society of America Bulletin*, *113*(12), 1580–1592. https://doi.org/10.1130/0016-7606(2001)113<1580:PTMATC>2.0.CO;2

Argus, D. F., Gordon, R. G., & DeMets, C. (2011). Geologically current motion of 56 plates relative to the no-net-rotation reference frame. *Geochemistry, Geophysics, Geosystems*, *12*(11), Q11001. https://doi.org/10.1029/2011GC003751

Average annual precipitation for California, USA (1900-1960) Data Basin. (2022). Retrieved from https://databasin.org/datasets/3fac6542263d4972af2f55dc13737f36/

Aydin, A., & Page, B. M. (1984). Diverse Pliocene-quaternary tectonics in a transform environment, San Francisco Bay region, California. *The Geological Society of America Bulletin*, *95*(11), 1303–1317. https://doi.org/10.1130/0016-7606(1984)95<1303:DPTIAT>2.0.CO;2

Baden, C. W., Shuster, D. L., Aron, F., Fosdick, J. C., Bürgmann, R., & Hilley, G. E. (2022). Bridging earthquakes and mountain building in the Santa Cruz Mountains, CA. *Science Advances*, *8*(8), eabi6031. https://doi.org/10.1126/sciadv.abi6031

Bay Area Census. (2020). Retrieved from http://www.bayareacensus.ca.gov/index.html

Bay Area Council Economic Institute. (2018). *Continuing growth and unparalleled innovation (Bay area economic profile No. 10)*. California. Retrieved from http://www.bayareaeconomy.org/report/continuing-growth-and-unparalleled-innovation/

Bürgmann, R., Arrowsmith, R., Dumitru, T., & McLaughlin, R. (1994). Rise and fall of the southern Santa Cruz Mountains, California, from fission tracks, geomorphology, and geodesy. *Journal of Geophysical Research*, *99*(B10), 20181–20202. https://doi.org/10.1029/94JB00131

Bürgmann, R., Segall, P., Lisowski, M., & Svarc, J. (1997). Postseismic strain following the 1989 Loma Prieta earthquake from GPS and leveling measurements. *Journal of Geophysical Research*, *102*(B3), 4933–4955. https://doi.org/10.1029/96JB03171

Castelltort, S., Goren, L., Willett, S. D., Champagnac, J.-D., Herman, F., & Braun, J. (2012). River drainage patterns in the New Zealand Alps primarily controlled by plate tectonic strain. *Nature Geoscience*, *5*(10), 744–748. https://doi.org/10.1038/ngeo1582

d'Alessio, M. A., Johanson, I. A., Bürgmann, R., Schmidt, D. A., & Murray, M. H. (2005). Slicing up the San Francisco Bay Area: Block kinematics and fault slip rates from GPS-derived surface velocities. *Journal of Geophysical Research*, *110*, B06403. https://doi.org/10.1029/2004JB003496

Duvall, A. R., & Tucker, G. E. (2015). Dynamic ridges and valleys in a strike-slip environment. *Journal of Geophysical Research: Earth Surface*, *120*, 2016–2026. https://doi.org/10.1002/2015JF003618

Ellsworth, W. L. (1990). *Earthquake history, 1769-1989* (p. 1515). United States Geological Survey, Professional Paper. Retrieved from https://www.osti.gov/biblio/5668161

Evans, E. L., Loveless, J. P., & Meade, B. J. (2012). Geodetic constraints on San Francisco Bay Area fault slip rates and potential seismogenic asperities on the partially creeping Hayward fault. *Journal of Geophysical Research*, *117*, B03410. https://doi.org/10.1029/2011JB008398

Field, E. H., Jordan, T. H., Page, M. T., Milner, K. R., Shaw, B. E., Dawson, T. E., et al. (2017). A synoptic view of the third uniform California earthquake rupture forecast (UCERF3). *Seismological Research Letters*, *88*(5), 1259–1267. https://doi.org/10.1785/0220170045

Geuzaine, C., & Remacle, J.-F. (2009). Gmsh: A 3-D finite element mesh generator with built-in pre- and post-processing facilities. *International Journal for Numerical Methods in Engineering*, *79*(11), 1309–1331. https://doi.org/10.1002/nme.2579

Goren, L., Fox, M., & Willett, S. D. (2014). Tectonics from fluvial topography using formal linear inversion: Theory and applications to the Inyo Mountains, California. *Journal of Geophysical Research: Earth Surface*, *119*, 1651–1681. https://doi.org/10.1002/2014JF003079

Graymer, R. W., Moring, B. C., Saucedo, G. J., Wentworth, C. M., Brabb, E. E., & Knudsen, K. L. (2006). *Geologic map of the San Francisco Bay region (USGS numbered series No. 2918)*. U.S. Geological Survey. Retrieved from http://pubs.er.usgs.gov/publication/sim2918

Hilley, G. E., Porder, S., Aron, F., Baden, C. W., Johnstone, S. A., Liu, F., et al. (2019). Earth's topographic relief potentially limited by an upper bound on channel steepness. *Nature Geoscience*, *12*(10), 828–832. https://doi.org/10.1038/s41561-019-0442-3

Hitchcock, C. S., & Kelson, K. I. (1999). Growth of late Quaternary folds in southwest Santa Clara Valley, San Francisco Bay area, California: Implications of triggered slip for seismic hazard and earthquake recurrence. *Geology*, *27*(5), 391–394. https://doi.org/10.1130/0091-7613(1999)027<0391:GOLQFI>2.3.CO;2

Huntington, K. W., Klepeis, K. A., & with 66 community contributors (Eds) (2018). *Challenges and opportunities for research in tectonics: Understanding deformation and the processes that link Earth systems, from geologic time to human time. A community vision document submitted to the U.S. National Science Foundation*. University of Washington. Retrieved from https://doi.org/10.6069/H52R3PQ5

Johnson, K. M., & Fukuda, J. (2010). New methods for estimating the spatial distribution of locked asperities and stress-driven interseismic creep on faults with application to the San Francisco Bay Area, California. *Journal of Geophysical Research*, *115*, B12408. https://doi.org/10.1029/2010JB007703

Kirby, E., & Whipple, K. X. (2012). Expression of active tectonics in erosional landscapes. *Journal of Structural Geology*, *44*, 54–75. https://doi.org/10.1016/j.jsg.2012.07.009

Langenheim, V. E., Jachens, R. C., Wentworth, C. M., Graymer, R. W., Stanley, R. G., McLaughlin, R. J., et al. (2015). A summary of the late Cenozoic stratigraphic and tectonic history of the Santa Clara Valley, California. *Geosphere*, *11*(1), 50–62. https://doi.org/10.1130/GES01093.1

Loveless, J. P. (2019). tribem: Boundary element code using triangular dislocation elements. *Zenodo*. https://doi.org/10.5281/zenodo.3333899

Marshall, S. T., Cooke, M. L., & Owen, S. E. (2009). Interseismic deformation associated with three-dimensional faults in the greater Los Angeles region, California. *Journal of Geophysical Research*, *114*, B12403. https://doi.org/10.1029/2009JB006439

McCalpin, J. P. (2009). *Paleoseismology*. Academic Press.

Mclaughlin, R. J., Langenheim, V. E., Schmidt, K. M., Jachens, R. C., Stanley, R. G., Jayko, A. S., et al. (1999). Neogene contraction between the San Andreas Fault and the Santa Clara Valley, San Francisco Bay Region, California. *International Geology Review*, *41*(1), 1–30. https://doi.org/10.1080/00206819909465130

Mongovin, D. D., & Philibosian, B. (2021). Creep on the Sargent Fault over the past 50 yr from alignment arrays with implications for slip transfer between the Calaveras and San Andreas Faults, California. *Bulletin of the Seismological Society of America*, *111*(6), 3189–3203. https://doi.org/10.1785/0120210041

Murray, M. H., & Segall, P. (2001). Modeling broadscale deformation in northern California and Nevada from plate motions and elastic strain accumulation. *Geophysical Research Letters*, *28*(22), 4315–4318. https://doi.org/10.1029/2001GL013373

National Research Council. (1994). *Practical lessons from the Loma Prieta earthquake*. The National Academies Press. Retrieved from https://www.nap.edu/catalog/2269/practical-lessons-from-the-loma-prieta-earthquake

Perron, J. T., & Royden, L. (2013). An integral approach to bedrock river profile analysis. *Earth Surface Processes and Landforms*, *38*(6), 570–576. https://doi.org/10.1002/esp.3302

Pollard, D. D., & with 25 community contributors (2003). In *New departures in structural geology and tectonics: A white paper resulting from a workshop held at Denver, Colorado, September 22nd and 23rd, 2002 sponsored by the tectonics Program, Earth Sciences Division, and National Science Foundation (GEO/EAR)*. Department of Geological and Environmental Sciences, Stanford University. Retrieved from https://www.researchgate.net/publication/291177404_Beyond_plate_tectonics_rheology_and_orogenesis_of_the_continents_in_new_departures_in_structural_geology_and_tectonics

Prescott, W. H., & Burford, R. O. (1976). Slip on the Sargent fault. *Bulletin of the Seismological Society of America*, *66*(3), 1013–1016. https://doi.org/10.1785/BSSA0660031013

Prescott, W. H., Lisowski, M., & Savage, J. C. (1981). Geodetic measurement of crustal deformation on the San Andreas, Hayward, and Calaveras Faults near San Francisco, California. *Journal of Geophysical Research*, *86*(B11), 10853–10869. https://doi.org/10.1029/JB086iB11p10853

Savage, J. C., Svarc, J. L., & Prescott, W. H. (1999). Geodetic estimates of fault slip rates in the San Francisco Bay area. *Journal of Geophysical Research*, *104*(B3), 4995–5002. https://doi.org/10.1029/1998JB900108

Schwartz, D. P., Lienkaemper, J. J., Hecker, S., Kelson, K. I., Fumal, T. E., Baldwin, J. N., et al. (2014). The earthquake cycle in the San Francisco Bay Region: A.D. 1600–2012. *Bulletin of the Seismological Society of America*, *104*(3), 1299–1328. https://doi.org/10.1785/0120120322

Schwartz, D. P., Pantosti, D., Okumura, K., Powers, T. J., & Hamilton, J. C. (1998). Paleoseismic investigations in the Santa Cruz Mountains, California: Implications for recurrence of large-magnitude earthquakes on the San Andreas Fault. *Journal of Geophysical Research*, *103*(B8), 17985–18001. https://doi.org/10.1029/98JB00701

Segall, P., & Lisowski, M. (1990). Surface displacements in the 1906 San Francisco and 1989 Loma Prieta earthquakes. *Science*, *250*(4985), 1241–1244. https://doi.org/10.1126/science.250.4985.1241

Shimazaki, K., & Nakata, T. (1980). Time-predictable recurrence model for large earthquakes. *Geophysical Research Letters*, *7*(4), 279–282. https://doi.org/10.1029/GL007i004p00279

State of California Department of Finance. (2020). Retrieved from http://www.dof.ca.gov/

Steer, P. (2021). Short communication: Analytical models for 2D landscape evolution. *Earth Surface Dynamics*, *9*(5), 1239–1250. https://doi.org/10.5194/esurf-9-1239-2021

Stock, J. D., & Montgomery, D. R. (1999). Geologic constraints on bedrock river incision using the stream power law. *Journal of Geophysical Research*, *104*(B3), 4983–4993. https://doi.org/10.1029/98JB02139

Sykes, L. R., & Jaumé, S. C. (1990). Seismic activity on neighbouring faults as a long-term precursor to large earthquakes in the San Francisco Bay area. *Nature*, *348*(6302), 595–599. https://doi.org/10.1038/348595a0

Tikoff, B., Blenkinsop, T., Kruckenberg, S. C., Morgan, S., Newman, J., & Wojtal, S. (2013). A perspective on the emergence of modern structural geology: Celebrating the feedbacks between historical-based and process-based approaches. *Geological Society of America Special Paper*, *500*, 65–119. https://doi.org/10.1130/2013.2500(03

Turner, R. C., Nadeau, R. M., & Bürgmann, R. (2013). Aseismic slip and fault interaction from repeating earthquakes in the Loma Prieta aftershock zone. *Geophysical Research Letters*, *40*(6), 1079–1083. https://doi.org/10.1002/grl.50212

Tuttle, M. P., & Sykes, L. R. (1992). Re-evaluation of several large historic earthquakes in the vicinity of the Loma Prieta and peninsular segments of the San Andreas fault, California. *Bulletin of the Seismological Society of America*, *82*(4), 1802–1820.

U. S. Geological Survey Staff. (1990). The Loma Prieta, California, earthquake: An anticipated event. *Science*, *247*(4940), 286–293. https://doi.org/10.1126/science.247.4940.286

Whipple, K. X., & Tucker, G. E. (1999). Dynamics of the stream-power river incision model: Implications for height limits of mountain ranges, landscape response timescales, and research needs. *Journal of Geophysical Research*, *104*(B8), 17661–17674. https://doi.org/10.1029/1999JB900120

Yu, E., & Segall, P. (1996). Slip in the 1868 Hayward earthquake from the analysis of historical triangulation data. *Journal of Geophysical Research*, *101*(B7), 16101–16118. https://doi.org/10.1029/96JB00806

References From the Supporting Information

Barnes, R., Lehman, C., & Mulla, D. (2014). Priority-flood: An optimal depression-filling and watershed-labeling algorithm for digital elevation models. *Computers & Geosciences*, *62*, 117–127. https://doi.org/10.1016/j.cageo.2013.04.024

Brocher, T. M., McCarthy, J., Hart, P. E., Holbrook, W. S., Furlong, K. P., McEvilly, T. V., et al. (1994). Seismic evidence for a lower-crustal detachment beneath San Francisco Bay, California. *Science*, *265*(5177), 1436–1439. https://doi.org/10.1126/science.265.5177.1436

Chéry, J. (2008). Geodetic strain across the San Andreas Fault reflects elastic plate thickness variations (rather than fault slip rate). *Earth and Planetary Science Letters*, *269*(3–4), 352–365. https://doi.org/10.1016/j.epsl.2008.01.046

Cooke, M. L., & Dair, L. C. (2011). Simulating the recent evolution of the southern big bend of the San Andreas Fault, Southern California. *Journal of Geophysical Research*, *116*, B04405. https://doi.org/10.1029/2010JB007835

Dair, L., & Cooke, M. L. (2009). San Andreas fault geometry through the San Gorgonio Pass, California. *Geology*, *37*(2), 119–122. https://doi.org/10.1130/G25101A.1

Ferrier, K. L., Huppert, K. L., & Perron, J. T. (2013). Climatic control of bedrock river incision. *Nature*, *496*(7444), 206–209. https://doi.org/10.1038/nature11982

Fox, M., Goren, L., May, D. A., & Willett, S. D. (2014). Inversion of fluvial channels for paleorock uplift rates in Taiwan. *Journal of Geophysical Research: Earth Surface*, *119*, 1853–1875. https://doi.org/10.1002/2014JF003196

Griffith, W. A., & Cooke, M. L. (2005). How sensitive are fault-slip rates in the Los Angeles basin to tectonic boundary conditions? *Bulletin of the Seismological Society of America*, *95*(4), 1263–1275. https://doi.org/10.1785/0120040079

Hall, N. T., Wright, R. H., & Clahan, K. B. (1999). Paleoseismic studies of the San Francisco Peninsula segment of the San Andreas Fault zone near Woodside, California. *Journal of Geophysical Research*, *104*(B10), 23215–23236. https://doi.org/10.1029/1999JB900157

Herbert, J. W., Cooke, M. L., & Marshall, S. T. (2014). Influence of fault connectivity on slip rates in southern California: Potential impact on discrepancies between geodetic derived and geologic slip rates. *Journal of Geophysical Research: Solid Earth*, *119*, 2342–2361. https://doi.org/10.1002/2013JB010472

Hilley, G. E., Mynatt, I., & Pollard, D. D. (2010). Structural geometry of Raplee Ridge monocline and thrust fault imaged using inverse Boundary Element Modeling and ALSM data. *Journal of Structural Geology*, *32*(1), 45–58. https://doi.org/10.1016/j.jsg.2009.06.015

Howard, A. D., & Kerby, G. (1983). Channel changes in badlands. *GSA Bulletin*, *94*(6), 739–752. https://doi.org/10.1130/0016-7606(1983)94<739:CCIB>2.0.CO;2

Langenheim, V. E., Schmidt, K. M., & Jachens, R. C. (1997). Coseismic deformation during the 1989 Loma Prieta earthquake and range-front thrusting along the southwestern margin of the Santa Clara Valley, California. *Geology*, *25*(12), 1091–1094. https://doi.org/10.1130/0091-7613(1997)025<1091:CDDTLP>2.3.CO;2

Maerten, F., Maerten, L., & Pollard, D. D. (2014). iBem3D, a three-dimensional iterative boundary element method using angular dislocations for modeling geologic structures. *Computers & Geosciences*, *72*, 1–17. https://doi.org/10.1016/j.cageo.2014.06.007

McLaughlin, R. J. (1974). The Sargent-Berrocal fault zone and its relation to the San Andreas Fault system in the southern San Francisco Bay region and Santa Clara Valley, California. *US Geological Survey Journal of Research*, *2*(5), 593–598.

McLaughlin, R. J., Clark, J. C., Brabb, E. E., Helley, E. J., & Colon, C. J. (2001). *Geologic maps and structure sections of the southwestern Santa Clara Valley and southern Santa Cruz Mountains, Santa Clara and Santa Cruz Counties, California (USGS numbered series No. 2373)*. U.S. Geological Survey. Retrieved from http://pubs.er.usgs.gov/publication/mf2373

Meade, B. J. (2007). Algorithms for the calculation of exact displacements, strains, and stresses for triangular dislocation elements in a uniform elastic half space. *Computers & Geosciences*, *33*(8), 1064–1075. https://doi.org/10.1016/j.cageo.2006.12.003

Page, B. M., Coleman, R. G., & Thompson, G. A. (1998). OVERVIEW: Late Cenozoic tectonics of the central and southern Coast Ranges of California. *The Geological Society of America Bulletin*, *110*(7), 846–876. https://doi.org/10.1130/0016-7606(1998)110<0846:OLCTOT>2.3.CO;2

Pritchard, D., Roberts, G. G., White, N. J., & Richardson, C. N. (2009). Uplift histories from river profiles. *Geophysical Research Letters*, *36*(24), L24301. https://doi.org/10.1029/2009GL040928

Roberts, G. G., & White, N. (2010). Estimating uplift rate histories from river profiles using African examples. *Journal of Geophysical Research*, *115*, B02406. https://doi.org/10.1029/2009JB006692

Roberts, G. G., White, N. J., Martin-Brandis, G. L., & Crosby, A. G. (2012). An uplift history of the Colorado Plateau and its surroundings from inverse modeling of longitudinal river profiles. *Tectonics*, *31*(4), TC4022. https://doi.org/10.1029/2012TC003107

Savage, J. C., Gan, W., Prescott, W. H., & Svarc, J. L. (2004). Strain accumulation across the Coast Ranges at the latitude of San Francisco, 1994–2000. *Journal of Geophysical Research*, *109*, B03413. https://doi.org/10.1029/2003JB002612

Savage, J. C., Simpson, R. W., & Murray, M. H. (1998). Strain accumulation rates in the San Francisco Bay area, 1972–1989. *Journal of Geophysical Research*, *103*(B8), 18039–18051. https://doi.org/10.1029/98JB01574

Schwartz, S. Y., Orange, D. L., & Anderson, R. S. (1990). Complex fault interactions in a restraining bend on the San Andreas Fault, southern Santa Cruz Mountains, California. *Geophysical Research Letters*, *17*(8), 1207–1210. https://doi.org/10.1029/GL017i008p01207

Segall, P. (2010). *Earthquake and volcano deformation*. Princeton University Press.

Shelef, E., & Hilley, G. E. (2013). Impact of flow routing on catchment area calculations, slope estimates, and numerical simulations of landscape development. *Journal of Geophysical Research: Earth Surface*, *118*, 2105–2123. https://doi.org/10.1002/jgrf.20127

Sorg, D. H., & McLaughlin, R. J. (1975). Geologic map of the Sargent-Berrocal fault zone between Los Gatos and Los Altos Hills, (Report No. 643). https://doi.org/10.3133/mf643

Stock, J. D., & Dietrich, W. E. (2003). Valley incision by debris flows: Evidence of a topographic signature. *Water Resources Research*, *39*(4), 1089. https://doi.org/10.1029/2001WR001057

Tarboton, D. G. (1997). A new method for the determination of flow directions and upslope areas in grid digital elevation models. *Water Resources Research*, *33*(2), 309–319. https://doi.org/10.1029/96WR03137

Thomas, A. L. (1993). *POLY3D: A three-dimensional, polygonal element, displacement discontinuity boundary element computer program with applications to fractures, faults, and cavities in the Earth's crust* (Master's thesis). Stanford University.

Turcotte, D. L., & Schubert, G. (2002). *Geodynamics* (2nd ed.). Cambridge University Press.

U.S. Geological Survey 3DEP Products & Services. (2019). Retrieved from https://www.usgs.gov/core-science-systems/ngp/3dep/about-3dep-products-services

U.S. Geological Survey, & California Geological Survey. (2021). Quaternary fault and fold database for the United States. [Data set]. Geo Gateway. https://doi.org/10.5066/F7S75FJM

Whipple, K. X., Hancock, G. S., & Anderson, R. S. (2000). River incision into bedrock: Mechanics and relative efficacy of plucking, abrasion, and cavitation. *GSA Bulletin*, *112*(3), 490–503. https://doi.org/10.1130/0016-7606(2000)112<490:RIIBMA>2.0.CO;2

Wobus, C., Whipple, K. X., Kirby, E., Snyder, N., Johnson, J., Spyropolou, K., et al. (2006). Tectonics from topography: Procedures, promise, and pitfalls. *Geological Society of America Special Paper*, *398*, 55–74. https://doi.org/10.1130/2006.2398(04

Zhang, E., Fuis, G. S., Catchings, R. D., Scheirer, D. S., Goldman, M., & Bauer, K. (2018). Reexamination of the subsurface fault structure in the vicinity of the 1989 moment-magnitude-6.9 Loma Prieta earthquake, central California, using steep-reflection, earthquake, and magnetic data (USGS Numbered Series No. 2018–1093). U.S. Geological Survey. https://doi.org/10.3133/ofr20181093